Contribution of QZSS with four satellites to multi-GNSS long baseline RTK

Article *in* Spatial Science · September 2019

DOI: 10.1080/14498596.2019.1646676

6 authors, including:

Yize Zhang
Tokyo University of Marine Science and Technology
48 PUBLICATIONS **116** CITATIONS
SEE PROFILE

Nobuaki Kubo
Tokyo University of Marine Science and Technology
103 PUBLICATIONS **470** CITATIONS
SEE PROFILE

Junping Chen
Chinese Academy of Sciences
103 PUBLICATIONS **687** CITATIONS
SEE PROFILE

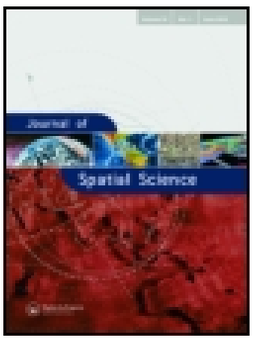

Journal of Spatial Science

ISSN: 1449-8596 (Print) 1836-5655 (Online) Journal homepage: https://www.tandfonline.com/loi/tjss20

Contribution of QZSS with four satellites to multi-GNSS long baseline RTK

Yize Zhang, Nobuaki Kubo, Junping Chen, Feng-Yu Chu, Hu Wang & Jiexian Wang

To cite this article: Yize Zhang, Nobuaki Kubo, Junping Chen, Feng-Yu Chu, Hu Wang & Jiexian Wang (2019): Contribution of QZSS with four satellites to multi-GNSS long baseline RTK, Journal of Spatial Science, DOI: 10.1080/14498596.2019.1646676

To link to this article: https://doi.org/10.1080/14498596.2019.1646676

Published online: 13 Sep 2019.

JOURNAL OF SPATIAL SCIENCE
https://doi.org/10.1080/14498596.2019.1646676

Taylor & Francis
Taylor & Francis Group

Contribution of QZSS with four satellites to multi-GNSS long baseline RTK

Yize Zhang[a,b], Nobuaki Kubo[a], Junping Chen[b,c], Feng-Yu Chu[a], Hu Wang[d] and Jiexian Wang[e]

[a]Department of maritime systems engineering, Tokyo University of Marine Science and Technology, Koto-ku, Tokyo, Japan; [b]Shanghai Astronomical Observatory Chinese Academy of Sciences, Shanghai, China; [c]Shanghai Key Laboratory of Space Navigation and Positioning Techniques, Shanghai, China; [d]Chinese Academy of Surveying and Mapping, Beijing, China; [e]College of Surveying and Geo-Informatics, Tongji University, Shanghai, China

ABSTRACT

In this contribution, we present the triple frequency long baseline RTK algorithm and assess the contribution of QZSS to multi-GNSS RTK. The impacts of multi-GNSS broadcast orbit errors, ionosphere, and troposphere errors on the long baseline RTK are analyzed. To assess the contribution of QZSS, multi-GNSS data are collected in Japan. The analysis of the results demonstrates that with the introduction of QZSS observations, the ambiguity dilution of precision of the long baseline RTK is considerably reduced in comparison with the GPS-only or GPS+Galileo scenarios. The convergence time and instantaneous RTK performance can be significantly improved when combined with other GNSS systems.

KEYWORDS

Long baseline RTK; partial ambiguity resolution; wide lane; ambiguity dilution of precision; time to first fix

1. Introduction

RTK is a well-known technique for achieving millimeter to centimeter-level positioning accuracy. In comparison with precision point positioning (PPP), RTK has the advantage of a lower dependence on the precision of a satellite's orbit and clock to achieve an instantaneous fixed solution for a short baseline using broadcast ephemeris, assuming that the difference of the satellite-dependent and atmosphere-dependent errors from the base station to rover station could be substantially eliminated. However, for medium or long baselines, the correlations of these common errors from satellite orbit, ionosphere, and troposphere differences decrease between two stations and is no longer negligible (Li *et al*. 2010a; Takasu and Yasuda 2010; Odolinski *et al*. 2014). Many researchers have investigated the performance of long baseline RTK considering troposphere and ionosphere differences. The conventional method uses ionosphere-free (IF) combination to eliminate ionosphere delay (Feng 2008). A wide lane (WL) or narrow lane (NL) combination can be used for integer ambiguity resolution (AR). However, IF combination doesn't effectively exploit ionosphere delay information by eliminating it, which could increase the time for the re-convergence of ambiguity after signal loss. Therefore, raw code and phase measurements are usually used, and the ionosphere delay is

CONTACT Nobuaki Kubo nkubo@kaiyodai.ac.jp

estimated as a parameter (Takasu and Yasuda 2010). To improve the ambiguity fixing rate, Li *et al*. (2014) improved this method by adding WL and NL ambiguity estimation.

With the development of other GNSS systems, such as Galileo, BeiDou, and QZSS, multi-GNSS RTK could significantly improve the positioning performance in ambiguity dilution of precision (ADOP), success rate, fixing rate, and accuracy (Chu and Yang 2014, Odolinski *et al*. 2015a, Li *et al*. 2017, Odolinski and Teunissen 2017). In addition, Galileo, BeiDou, and QZSS provide a three-frequency or even a four-frequency signal. GPS Block IIF also supports an L5 signal besides L1 and L2, which indicates that multi-frequency positioning is very promising for future multi-GNSS. Using a triple-frequency, more linear combinations could be formed and would benefit long baseline RTK. For instance, the ambiguity of extra-wide-lane (EWL) could be fixed by integer rounding because of the long wavelength of EWL (Feng and Li 2008). Ambiguity fixed EWL observations can be regarded as new code measurements with much smaller noise that could facilitate fast ionosphere and ambiguity estimation (Li *et al*. 2010b, Chu *et al*. 2016).

As a regional augmentation system to GPS, QZSS announced the provision of official service from November 2018. Consisted of 3 IGSO satellites and 1 GEO satellite, QZSS was designed to cover regions of East Asia and Oceania centered about Japan and could enhance other GNSS systems in terms of availability and positioning performance (JAXA 2017). Takasu *et al*. (2009) first evaluated the effect of a simulated 7-QZSS satellite constellation regarding single point positioning (SPP) and RTK. Kubo *et al*. (2011) reported on the improvement of RTK using real GPS/QZSS data after the launch of the first QZSS satellite. Since then, the performance of multi-GNSS combined with QZSS has been investigated (Kitamura *et al*. 2014, Odolinski *et al*. 2014, 2015a, Odijk *et al*. 2017, Odolinski and Teunissen 2017). However, the contribution of QZSS was not analyzed in detail, possibly because there was only one QZSS satellite at the time. Recently, Zhang *et al*. (2018a) and Zhang *et al*. (2018b) assessed the performance of QZSS augmenting GPS and BDS including short baseline RTK in the Asia-Pacific area using the four-satellite QZSS constellation. Zaminpardaz *et al*. (2018) explored the standalone RTK performance and considered the troposphere impact on a 8 km baseline. Although it is expected that QZSS could also benefit medium or long baseline RTK, there are limited relevant studies on the newest QZSS constellation with four satellites.

To assess the contribution of QZSS in long baseline RTK, this study presents the first result of QZSS combined multi-GNSS long baseline RTK performance in Japan. A brief introduction of the triple-frequency based long baseline RTK algorithm is described in Section 2. Then, the impacts of double differenced satellite orbit, troposphere, and ionosphere delay in the long baseline are investigated using real data. In addition to the RTK performance of different lengths of baselines, the contribution of the QZSS system in terms of ADOP, RTK accuracy, convergence performance, and instantaneous ambiguity resolution performance is evaluated. Finally, the main points are presented in the conclusion.

2. Long baseline RTK algorithm

2.1. Conventional RTK model

The double-differenced (DD) observation between base and rover stations can be simplified as (Odolinski *et al*. 2015b):

$$\begin{aligned}\nabla\Delta P_f &= \nabla\Delta\rho + m\nabla\Delta T + \alpha_f\nabla\Delta I + \nabla\Delta\varepsilon_{P_f}\\ \nabla\Delta\Phi_f &= \nabla\Delta\rho + m\nabla\Delta T - \alpha_f\nabla\Delta I + \lambda_f\nabla\Delta N + \nabla\Delta\varepsilon_{P_f}\end{aligned}, \tag{1}$$

where $\nabla\Delta$ is the DD operator, λ is the wavelength on frequency f, P and Φ represent the code and carrier phase observations, respectively, ρ is the geometry distance between the receiver and satellite, T represents the zenith troposphere delay, m is the mapping function, I represents the slant ionosphere delay, α is the frequency-depended coefficient, N denotes the carrier phase ambiguity, andε_P and ε_P include other modelled errors, multipath, and observation noise.

For short baseline RTK (<10 km), the double-differenced troposphere and ionosphere delay are small enough that they can be ignored. Therefore, the remaining parameter to be estimated is the coordinate of the rover station and the double-differenced ambiguity. This is the so-called ionosphere-fixed model (Odijk 2000, Teunissen and Montenbruck 2017). For long baseline RTK, the zenith troposphere delay and slant ionosphere delay cannot be canceled and must be estimated as parameters. If the ionosphere delay can be incorporated in some form of constraint, the model is referred to as the ionosphere-weighting model (Odijk 2000).

After linearization of Equation (1), the observation equation can be written in compact form as follows:

$$\begin{aligned} y &= Gx\\ R &= E[\varepsilon\varepsilon^T],\ \ E[\varepsilon] = 0\end{aligned} \tag{2}$$

where **y** is the pre-fit residuals after linearization and **G** is the design matrix, **x** represents the unknown parameters including the baseline components, troposphere, ionosphere, and ambiguity in the long baseline RTK. **R** is the variance-covariance matrix calculated from an elevation dependent stochastic model:

$$\sigma = \left(0.5 + \frac{0.5}{\sin(Ele)}\right)\sigma_0 \tag{3}$$

where *Ele* is the satellite elevation and σ_0 is the observation noise in the zenith direction, which is set as 0.3 m and 0.3 cm for code and carrier phase observations, respectively.

The parameters can be estimated by applying classical Kalman Filtering (KF) as follows:

$$\begin{aligned}\hat{\mathbf{x}}_k^- &= \Phi_{k-1}\hat{\mathbf{x}}_{k-1}^-\\ \mathbf{P}_{\hat{\mathbf{x}}_k}^- &= \Phi_{k-1}\mathbf{P}_{\hat{\mathbf{x}}_{k-1}}\Phi^{\mathbf{T}}{}_{k-1} + \mathbf{Q}_{k-1}\\ \mathbf{K}_k &= \mathbf{P}_{\hat{\mathbf{x}}_k}^-\mathbf{G}^T{}_k\left[\mathbf{G}_k\mathbf{P}_{\hat{\mathbf{x}}_k}^-\mathbf{G}_k{}^T + \mathbf{R}_k\right]^{-1}\\ \hat{\mathbf{x}}_k &= \hat{\mathbf{x}}_k^- + \mathbf{K}_k\left[\mathbf{y}_k - \mathbf{G}_k\hat{\mathbf{x}}_k^-\right]\\ \mathbf{P}_{\hat{\mathbf{x}}_k} &= [\mathbf{I} - \mathbf{K}_k\mathbf{G}_k]\mathbf{P}_{\hat{\mathbf{x}}_k}^-\end{aligned} \tag{4}$$

where Φ is named the transition matrix between epoch k-1 and k and defines the propagation between the estimated parameter $\hat{\mathbf{x}}$ and predicted parameter $\hat{\mathbf{x}}^-$, **Q** is the process noise matrix between the variance-covariance matrix **P** and the predicted $\mathbf{P}^-$. **K** is the well-known Kalman Gain matrix that indicates the change between the predicted and estimated parameters.

The parameter could be estimated epoch-wise using the KF. Once the float ambiguity is fixed to an integer value using the LAMBDA method, the fixed solution and variance-covariance matrix can be updated as follows (Teunissen 1995; Verhagen and Li 2012):

$$\begin{aligned}\breve{\mathbf{b}} &= \hat{\mathbf{b}} - \mathbf{Q}_{\hat{\mathbf{b}}\hat{\mathbf{a}}}\mathbf{Q}_{\hat{\mathbf{a}}\hat{\mathbf{a}}}^{-1}(\hat{\mathbf{a}} - \breve{\mathbf{a}}) \\ \mathbf{Q}_{\breve{\mathbf{b}}\breve{\mathbf{b}}} &= \mathbf{Q}_{\hat{\mathbf{b}}\hat{\mathbf{a}}} - \mathbf{Q}_{\hat{\mathbf{b}}\hat{\mathbf{a}}}\mathbf{Q}_{\hat{\mathbf{a}}\hat{\mathbf{a}}}{}^{-1}\mathbf{Q}_{\hat{\mathbf{a}}\hat{\mathbf{b}}}\end{aligned} \tag{5}$$

where $\mathbf{Q}$ is part of the variance-covariance matrix, $\hat{\mathbf{a}}$is the float ambiguity, $\breve{\mathbf{a}}$ is the fixed ambiguity and$\mathbf{b}$represents other real-valued parameters including coordinates.

However, with the increase of the satellite number in multi-GNSS, it is not easy to fix all ambiguities using the traditional LAMBDA method, especially for long baseline RTK when the model strength is too weak (Verhagen and Teunissen 2013, Odolinski *et al*. 2015b). To overcome this problem, an improved partial ambiguity resolution (PAR) is proposed (Teunissen *et al*. 1999; Verhagen and Li 2012). Research has shown that PAR benefits long baseline RTK in terms of the convergence time and ambiguity fixing success rate (Parkins 2011, Gao *et al*. 2015, Zhang *et al*. 2016). In this study, a data driven with two-step criterion PAR method is adopted (Hou *et al*. 2016).

2.2. Wide-lane and extra-wide-lane observations

For the new generation of GPS satellites, observation data at L1, L2, and L5 frequencies are available. The wavelength of WL and EWL ambiguity is 0.86 m and 5.86 m, respectively (Feng and Li 2008; Gao *et al*. 2015), which indicates that it is easy to fix the ambiguity, although it also amplifies ionosphere and observation noise. For WL AR, the LAMBDA method can be applied, whereas integer rounding is sufficient for EWL AR. In comparison with raw L1/L2 AR, WL AR is easier to fix and is, therefore, helpful for raw L1/L2 AR.

For triple-frequency GNSS data, EWL ambiguity can be fixed by simply rounding to the nearest integer using the geometry-free model (Gao *et al*. 2015). Then, EWL observation can be regarded as code measurement, which could be useful for fast WL AR. Unlike EWL AR, geometry-free WL AR is at risk to fix ambiguity by simple rounding method due to the noise from code measurement. Therefore, it is usually based on a geometry-based approach. Based on EWL observation, the WL AR model can be expressed as

$$\begin{bmatrix} V_{P_1} \\ V_{P_2} \\ V_{WL} \\ V_{EWL} \end{bmatrix} = \begin{bmatrix} B & 0 \\ B & 0 \\ B & I \\ B & 0 \end{bmatrix} \begin{bmatrix} X \\ N_{WL} \end{bmatrix} \tag{6}$$

where V is the pre-fit residuals of the observation vector, B is the geometry vector of the baseline coordinate X, and I is a unit vector of WL ambiguity N_{WL}.

In Equation (6), it should be noted that the effect of double-differenced ionosphere delay is not considered. For a certain baseline at a specific cut-off elevation, the impact of the ionosphere in WL AR can be ignored. The detailed reason will be discussed in the next section.

After fixing the WL ambiguity, the WL observation could be again regarded as a code measurement with much smaller noise than the raw code measurement. Therefore, the WL assisted raw long baseline RTK model is as follows:

$$\begin{bmatrix} V_{P_1} \\ V_{P_2} \\ V_{L_2} \\ V_{L_1} \\ V_{WL_{fix}} \end{bmatrix} = \begin{bmatrix} B & 0 & 0 & m & I \\ B & 0 & 0 & m & \frac{f_1^2}{f_2^2} I \\ B & I & 0 & m & -I \\ B & 0 & I & m & -\frac{f_1^2}{f_2^2} I \\ B & 0 & 0 & m & \frac{f_1}{f_2} I \end{bmatrix} \begin{bmatrix} X \\ N_{L_1} \\ N_{L_2} \\ Trop \\ Ion \end{bmatrix} \tag{7}$$

where WL_{fix} denotes the WL observation after ambiguity fixing, m denotes the mapping function of the troposphere, and Trop and Ion stand for the estimated zenith troposphere and slant ionosphere delay, respectively.

2.3. Troposphere and ionosphere weighting

With the additional estimated parameters including troposphere and ionosphere in long baseline RTK, the correlation among different kinds of parameters increases. As such, more time is required for ADOP to convergence to a sufficiently small level (Odijk and Teunissen 2008, Odolinski *et al*. 2015b). In Equation (7), the double-differenced troposphere and ionosphere are estimated together with station coordinates and ambiguity. To strengthen the AR model, an appropriate constraint could be added to an ionosphere-weighting model for long baseline RTK for fast convergence and correct AR in KF.

The newest global troposphere models, such as GPT2w, have a precision of 5 cm (Böhm *et al*. 2015). For the residual troposphere and ionosphere delay, as the epoch-difference troposphere and ionosphere delay vary within a certain value, which implies that they could be estimated as random walk parameters with a defined process noise in KF.

Given that troposphere error is distance and height related (Teunissen and Montenbruck 2017), after numerous experiments over Japan, the zenith troposphere constraint and random walk noise in each epoch are applied as follows:

$$\begin{aligned} P_{trop_0} &= \left(\log(1 + D \cdot 5 \cdot 10^{-4}) \cdot 0.05 + H \cdot 5 \cdot 10^{-5}\right) \\ Q_{trop} &= \left(\log(1 + D \cdot 10^{-5}) \cdot 0.02 + H \cdot 10^{-5}\right) / \sqrt{3600 \cdot \Delta t} \end{aligned} \tag{8}$$

where D represents the station distance, H is the height difference in meter and Δt is the epoch time difference in second.

Taking a baseline of 100 km with a height difference of 100 m as an example, according to Equation (8), the constraint on the troposphere is set as 0.2 m and the process noise is $0.015m/\sqrt{h}$.

For ionosphere delay, the vertical difference is between 2–50 ppm depending on the station latitude and solar activity (Wanninger 1993, Foster 2000). Considering that the estimated ionosphere is the slant delay, the constraint and random walk noise on the ionosphere should be modeled not only by the baseline length and latitude dependence but should also be elevation related. In this study, it is roughly expressed as follows:

$$\begin{aligned} P_{iono0} &= \left(D \cdot 5 \cdot 10^{-6} \cdot \exp((90 - lat)/50 - 1)\right)/\sin(ele) \\ Q_{iono} &= \left(D \cdot 5 \cdot 10^{-6} \cdot \exp((90 - lat)/50 - 1)\right)/\sin(ele)\sqrt{3600 \cdot \Delta t} \end{aligned} \tag{9}$$

where lat is the average latitude of two stations and ele is the elevation of the satellite.

For a baseline of 100 km at a latitude of 35°, the zenith ionosphere constraint and random walk step on the vertical are 0.55 m and $0.55\text{m}/\sqrt{h}$, respectively, i.e., approximately 5.5 ppm. This maps to 1.62 m and $1.62\text{m}/\sqrt{h}$at an elevation of 20°. When the station is in the equatorial region, the magnitude at the vertical is approximately 11 ppm. However, it should be noted that Equation (9) does not consider the factor of solar activity.

2.4. Triple frequency long baseline RTK

To summarize this section, the flowchart of triple frequency long baseline RTK could be described as shown in Figure 1. According to the figure, the WL normal equation is formed according to the geometry-based WL observation and geometry-free EWL observation, by setting an appropriate cut-off elevation and applying PAR, it is possible to fix the WL ambiguity. Once the WL ambiguity is fixed, it can be regarded as a 'pseudo-range' observation in combination with the raw code and carrier phase observation for

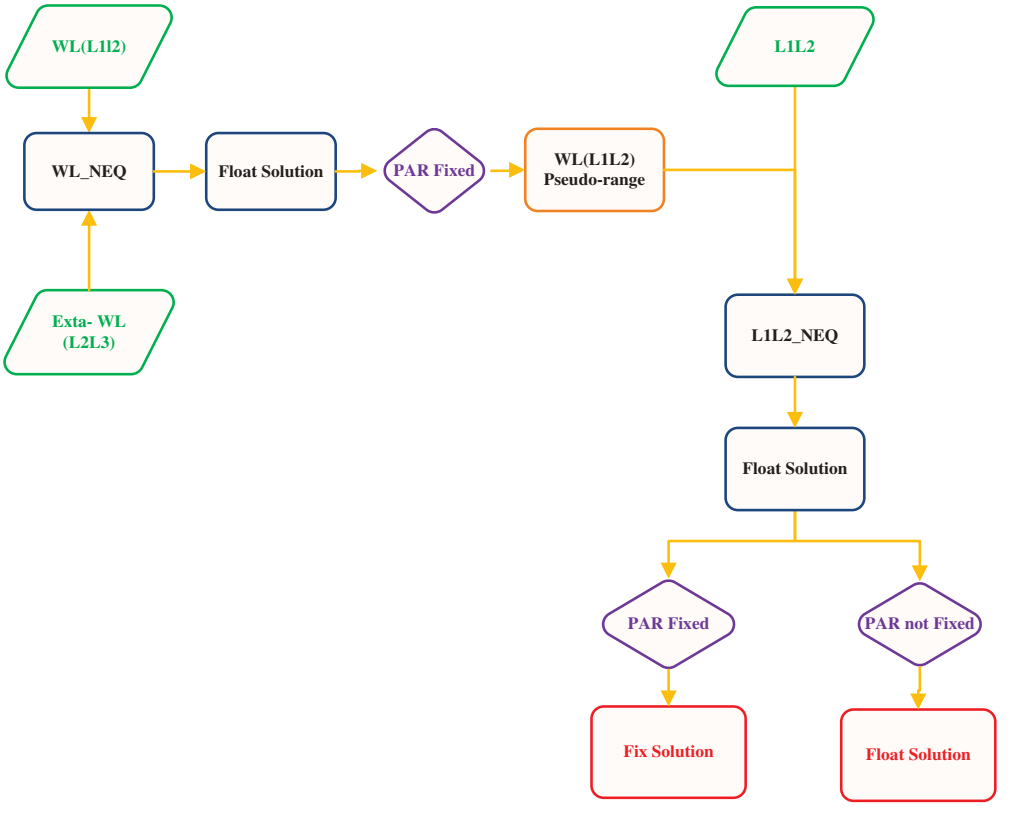

Figure 1. Flow chart of triple frequency long baseline RTK.

the L1 and L2 frequency. Using PAR, the ambiguity can be resolved, and the fixed solution is derived. Otherwise, the output would be the float solution.

3. Experiment setup and analysis

To validate the contribution of QZSS in long baseline RTK, four pairs of baselines variations from 60–200 km near Tokyo on November 10th, 2018 were selected and the location of the stations are depicted in Figure 2. These stations are operated by the Geospatial Information Authority of Japan (GSI) and they are all equipped with a Trimble NetR9 receiver at a data sampling of 30 s, which can receive GPS+GLONASS+Galileo +QZSS data (No BDS data is provided). Given that GLONASS is affected by inter-frequency bias (Wanninger 2012), in this study, we use GPS+Galileo+QZSS data for analysis. According to Odijk and Teunissen (2013) and Odijk *et al*. (2017), there exists a differential inter-system bias (DISB) in both code and phase for mix multi-GNSS RTK. However, for identical receivers, this DISB can be ignored. For the selected baselines in this study, we regard GPS and QZSS as the same system, and the DISB is absent at the same frequency of L1, L2, and L5. For Galileo, it is treated as a standalone system.

To fully understand the difference between short and long baseline RTK, the projected impacts of satellite orbit, troposphere and ionosphere errors on long baselines will be analyzed in this section.

3.1. Broadcast orbit difference

Generally, long baseline RTK adopts rapid or ultra-rapid precise orbit in post-processing to reduce the impact from satellite orbit difference. For real-time users, broadcast ephemeris is more convenient to access because it doesn't require real-time orbit and

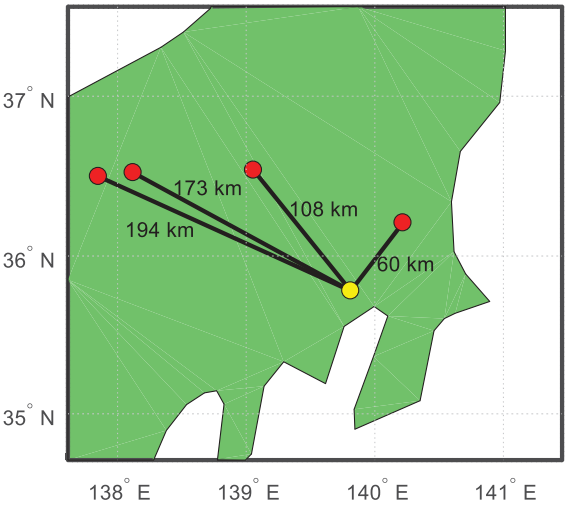

Figure 2. Four selected baselines near Tokyo. The yellow point is the base station and the red points represent four rover stations.

clock correction streams. Therefore, it is necessary to analyze the impact of broadcast orbit in long baseline RTK.

Although the satellite clock error can be ideally eliminated after station difference, the satellite orbit error cannot be ignored because of the line of sight (LOS) difference from each station. Theoretically, the impact on LOS from satellite orbit can be expressed as follows (Teunissen and Montenbruck 2017):

$$\Delta r < \frac{D}{S} \cdot \Delta s \tag{10}$$

where Δs denotes the satellite orbit error and Δr is its bias in LOS, D represents the baseline length and S is the geometry distance from the satellite to the receiver. Using this equation, we can estimate that an orbit error of 0.5 m on a baseline of 100 km has an impact of at most 0.23 cm difference (assuming the geometry distance is 22,000 km).

To validate the impact with real data, the two baselines at 60 km and 194 km were selected as an example, which is the extreme case of the four long baselines. The IGS final orbit and broadcast orbit were used to compare the double-differenced error in LOS. The 12-hour difference of the GPS/Galileo/QZSS is shown in Figure 3.

From the figure, it is evident that for the 60 km baseline, most of the double-differenced orbit errors for GPS, Galileo, and QZSS are within 0.5 cm, except for J07, a GEO satellite of QZSS. When the baseline length is extended to 194 km, most of the difference is within 1 cm, whereas for Galileo, the value is still well below 0.5 cm. This indicates that the orbit error of Galileo is better than that of GPS or QZSS, which has been proven by Montenbruck *et al*. (2017). It should be pointed out that the jumps of the difference in the figure is due to the change of the pivot satellite or the broadcast ephemeris. For instance, as shown in the dashed rectangle of 60 km baseline difference of QZSS and GPS, the pivot satellite changes from J02 to G32 at 07:34:30 and leads to a 2 mm jump for all GPS and QZSS satellites. Due to the ephemeris change at 07:00:00 of

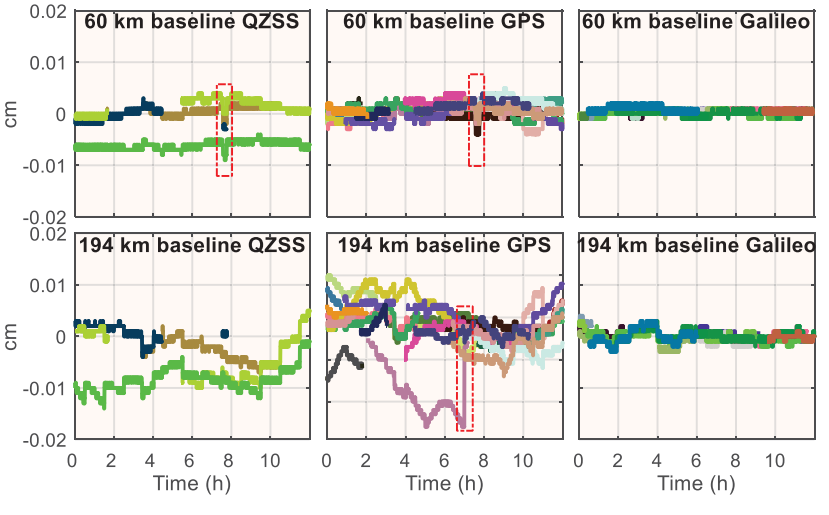

Figure 3. Broadcast orbit difference for baselines of 60 km (top) and 194 km (bottom). The three subplots from left to right are for QZSS, GPS, and Galileo, respectively. The jumps in the results are due to the change of the pivot satellite or the broadcast ephemeris.

G20, the difference on 194 km baseline reduces from −2.6 cm to −0.7 cm. Nevertheless, the magnitude of the orbit difference is sufficiently small and can be ignored for baselines less than 200 km. Therefore, the broadcast ephemeris is used in this study.

3.2. Troposphere difference

As previously indicated, the zenith troposphere delay can be corrected using a precise troposphere model at a precision of 5 cm. For RTK within a certain distance, the troposphere difference would be smaller because it is spatially correlated. However, the difference may be amplified after mapping to the slant direction, especially for satellites at low elevation. For float solutions like PPP, the influence of this mapping enlargement could be reduced by appropriate observation weighting. However, for integer AR solutions in RTK, the slant troposphere error affects AR performance.

Precise double-differenced troposphere error can be derived by fixing the station coordinates provided by GSI daily solutions and applying precise IGS final orbits. Figure 4 represents a plot of a one-day slant troposphere difference for the four baselines. With the decrease in the satellite elevation, the troposphere difference significantly increases due to the troposphere mapping factor. For a baseline of 60 km, the maximum troposphere difference is within 10 cm at an elevation of 10°. With the increase in the baseline length, the troposphere difference increases. This is expected as the spatial correlation of the troposphere decreases. The result also indicates that the troposphere difference can be estimated as a random walk model, and the setting of the troposphere constraint in Equation (8) is quite loose. For WL AR in Equation (6), the troposphere can still be ignored at an elevation above 20° for baselines within 200 km.

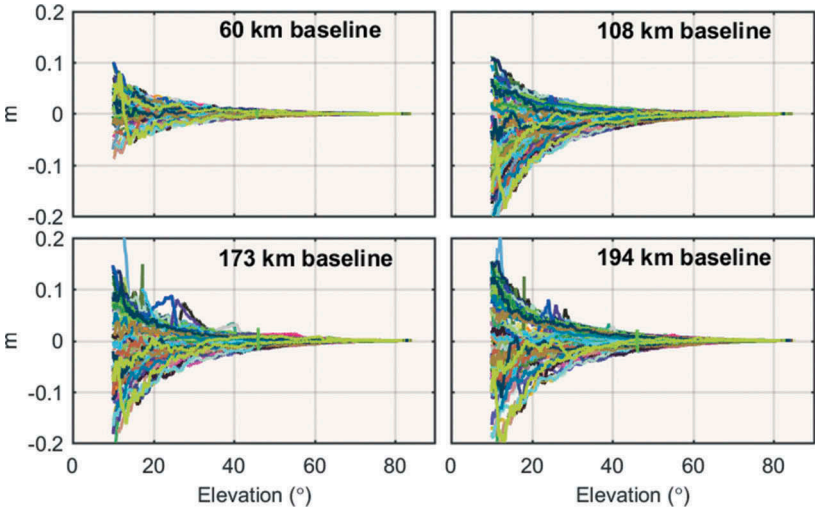

Figure 4. Troposphere difference for four baselines ranging from 60 km to 194 km at a cut-off elevation of 10°. The x label represents the satellite elevation.

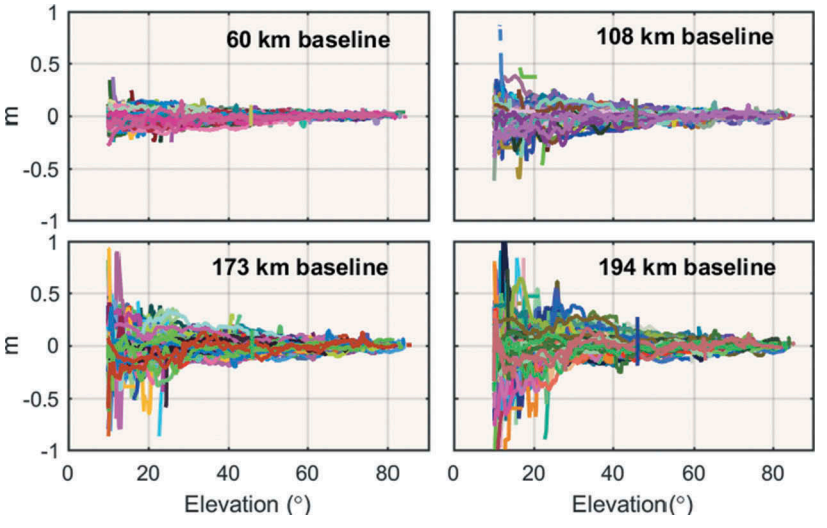

Figure 5. Ionosphere difference for four baselines ranging from 60 km to 194 km at a cut-off elevation of 10°. The x label represents satellite elevation.

3.3. Ionosphere difference

Compared with the troposphere, the ionosphere difference is usually considered to have a much more severe impact in long baseline RTK (Gao *et al*. 2015; Teunissen and Montenbruck 2017). By correcting the troposphere difference and fixing the station coordinates, the ionosphere difference and the ambiguity can be obtained. Similar to the troposphere, the difference for the four baselines is presented in Figure 5 for the one-day result.

Similarly, it can be observed that the ionosphere difference also exhibits an elevation depending on the relationship, and the magnitude differs at the length of the baseline. For the 60 km baseline, the ionosphere difference is within 0.3 m, while it can exceed 1 m for the 194 km baseline. For WL AR, users should carefully choose the cut-off elevation when the ionosphere-fixed model is applied. For a tolerance of 20 cm ionosphere difference, a cut-off elevation of 20° is suitable for 60 km baseline, while for the 194 km baseline, this threshold should be higher than 40°.

4. Contribution of QZSS in long baseline RTK

Section 3 proves that broadcast ephemeris difference can be ignored for baselines within 200 km, whereas the troposphere and ionosphere difference must be estimated as parameters in long baseline RTK. In this section, we present the contribution of QZSS in long baseline RTK based on the algorithm presented in Section 2.

4.1. Multi-GNSS tracking analysis

Using the data collected on the base station, the satellite number and elevation change are depicted in Figures 6 and 7. It is evident that there are always three or four QZSS

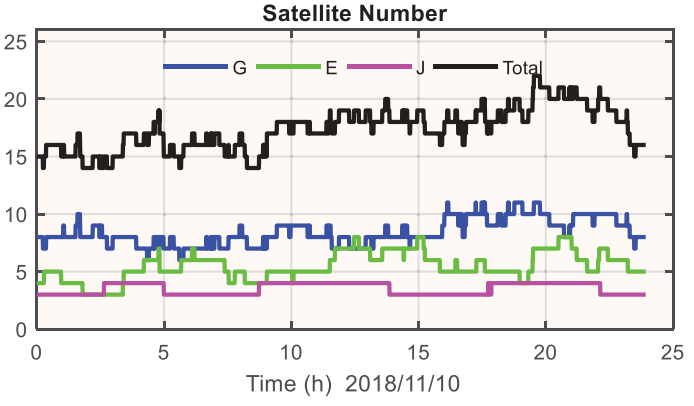

Figure 6. Visible satellite number at the base station with a cut-off elevation of 10°. G denotes GPS, E denotes Galileo and J denotes QZSS.

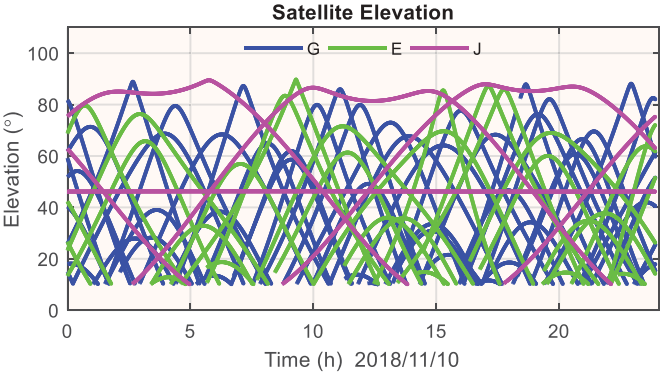

Figure 7. Satellite elevation change at the base station with a cut-off elevation of 10°.

satellites near Tokyo and more often than not, one of the IGSO satellites of QZSS is the highest elevation satellite. This is from the unique design of QZSS to stay for longer periods for the region of Japan (JAXA 2017). From Figure 6, it is evident that there are currently not many Galileo satellites over Japan. For the following analysis of multi-GNSS RTK, Galileo is combined with GPS and QZSS.

The GEO satellite of QZSS is always at an elevation of 46° at the base station. Based on the GNSS View (http://app.qzss.go.jp/GNSSView/gnssview.html), it can be determined that the satellite elevation of the QZSS GEO satellite ranges from 25° to 55° over mainland Japan. At Okinawa (most southern island of Japan), the elevation of the GEO satellite is 60° and one can always observe 4 QZSS satellites at a cut-off elevation of 10°. This is expected to contribute to positioning performance in combination with other GNSS systems.

To further illustrate the contribution of QZSS on the positioning model, the position dilution of precision (PDOP) value of QZSS combined with GPS and Galileo at the base station is plotted in Figure 8. When combined with QZSS, the mean PDOP improves from 1.51 to 1.23 for GPS, whereas for GPS+Galileo, the benefit is 1.10 versus 0.98. From

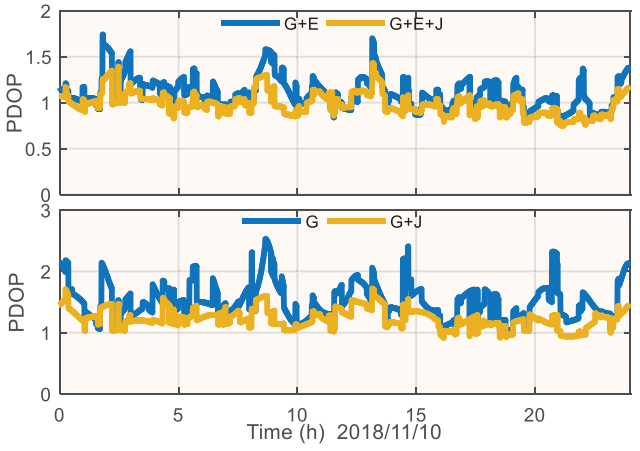

Figure 8. PDOP value for different GNSS combinations at the base station with a cut-off elevation of 10°. The upper subplot compares GPS+ Galileo and GPS+Galileo+QZSS, and the lower subplot compares GPS and GPS +QZSS.

Figure 8, it can be determined that after the combination with QZSS, the PDOP change becomes much smoother, especially in the case of GPS.

In the case of AR, ADOP is a critical concept that describes the success rate of AR. According to Teunissen (1997), ADOP can be defined as

$$ADOP = \sqrt{|Q_{\hat{a}}|^{\frac{1}{n}}} \ (cycle) \tag{11}$$

where $Q_{\hat{a}}$ is the variance-covariance matrix of float ambiguities, $|\cdot|$ is the determinant of the matrix, and n is the dimension of the ambiguity vector.

As determined by Odijk and Teunissen (2008), if ADOP is smaller than 0.14 cycles, the AR success rate is larger than 0.99.

To analyze the contribution of QZSS, the ADOP value is computed using the 60 km baseline in the long baseline RTK mode introduced in Section 2. For a better comparison, the Kalman Filter is re-initialized every half hour and the results of the first four sessions are depicted in Figure 9. Based on a comparison, it can be shown that the convergence of ADOP approaches 0.14 cycles much quicker after combining with QZSS in the case of GPS and Galileo. The one-day statistical result shows that with the contribution of QZSS, the convergence time of ADOP to 0.14 cycles decrease from 11.5 min to 5.4 min for GPS and from 6.4 min to 4.2 min for GPS+Galileo, which would undoubtedly accelerate the AR convergence time for long baseline RTK. It is interesting to note that the contribution of QZSS is higher than Galileo on GPS, although more Galileo satellites can be tracked than QZSS in Japan. This may because that GPS and QZSS are regarded as the same system and they share the same pivot satellite, while Galileo is a standalone system.

4.2. Multi-GNSS long baseline RTK performance

Following the algorithm described in Section 2, the RTK result can be obtained for the four baselines. According to the analysis in Section 3, the cut-off elevation is set as 40° in

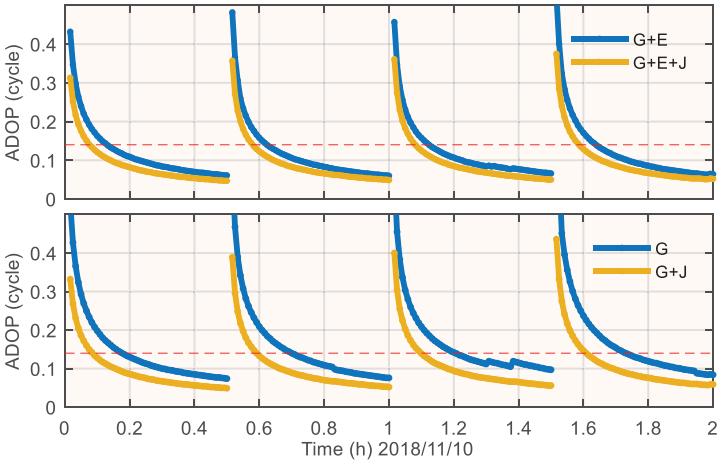

Figure 9. ADOP value for different GNSS combination. The red dashed line refers to an ADOP value of 0.14 cycles. The filter is re-initialized every half hour. The upper subplot compares GPS+Galileo and GPS+Galileo+QZSS, and the lower subplot compares GPS and GPS +QZSS.

the step of WL AR. By applying a continuous AR mode in the Kalman Filter (Takasu and Yasuda 2010), the minimum success rate is set as 0.99 in PAR (Verhagen and Li 2012) and the threshold of the ratio is set as 2.0 because the model strength is not very strong (Verhagen and Teunissen 2013). To reduce the impact of noise from low elevation satellites, the cut-off elevation is set as 10° for the float solution of the Kalman Filter and 20° in the procedure of ambiguity fixing.

To evaluate the RTK performance, the AR fixing rate is defined as follows:

$$fixing\_rate = \frac{n_{fix}}{n} \tag{12}$$

where n_{fix} is the correct fixed solution number and n is the total epoch number. The correct fixed solution implies that the ratio value is higher than 2.0 and the positioning error is less than 20 cm compared to the post-processed reference coordinate provided by GSI.

Figure 10 summarizes the continuous RTK results including positioning RMS in the horizontal and vertical directions (fixed solutions) and fixing rate using the 24 h data on November 10th, 2018. For a specific observation of long baseline RTK performance, the GPS-only and GPS+QZSS RTK performance at the 173 km baseline are also plotted in Figure 11.

From Figures 10 and 11, it can be determined that with the increase of the baseline length, the RTK precision and fixing rate would decrease slightly. Among all the different GNSS combinations, GPS-only long baseline RTK shows the worst result. When QZSS is combined, the performance greatly improves in terms of positioning accuracy and fixing rate. Nevertheless, the overall precision in RMS is within 2 cm in the horizontal and 4 cm in the vertical, and the fixing rate is also higher than 97%. The float solution mainly comes from the convergence period. Meanwhile, it should be noted that for long baseline RTK, given that the model strength is usually too weak, this would lead to a wrong fix and false rejection in LAMBDA (Verhagen and Teunissen 2013), especially for

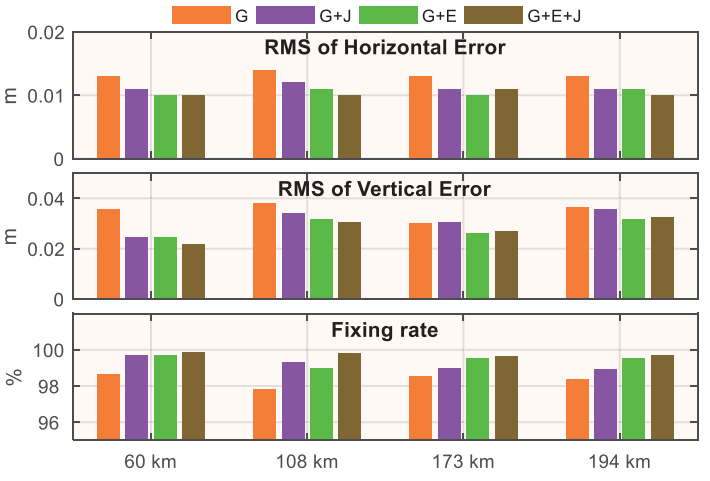

Figure 10. Continuous long baseline RTK statistic of four baselines: RMS of horizontal error (top); RMS of vertical error (middle); Fixing rate (bottom).

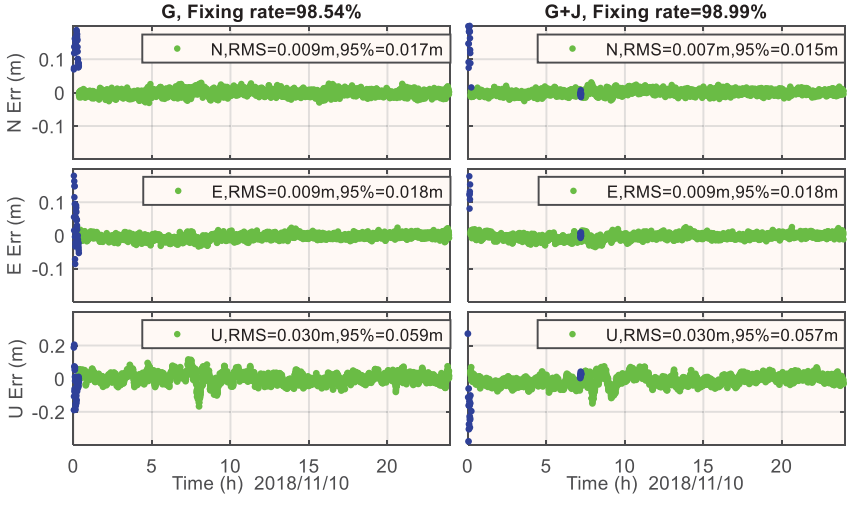

Figure 11. RTK performance for the 173 km baseline of GPS (left) and GPS+QZSS (right). The three subplots from top to bottom mean positioning error at North, East and Up direction. The blue point represents the float solution and the green point represents the fixed solution after LAMBDA.

our strategy of data-driven PAR, which can also be observed in Figure 11. However, the establishment of a more reliable AR decision strategy is beyond the discussion of this paper.

4.3. Convergence performance

For long baseline RTK, users may be more concerned about the convergence performance, or the time to first fix (TTFF). Although the analysis in Figure 9 already demonstrates that the convergence time of the ADOP value would significantly speed up with

the contribution of QZSS and the fixed solution could be derived within several minutes, it is still necessary to investigate the general convergence performance base on statistical positioning result.

To evaluate such performance, we re-initialize the long baseline RTK every 30 minutes. For each baseline, there are 48 sessions per day. The TTFF performance is executed for each session and the correct fixing rate of the four baselines for different GNSS combination are compared in Figure 12. Figure 13 gives detailed vertical positioning results for each session by comparing GPS+Galileo and GPS+Galileo+QZSS at the 173 km baseline. As the float solution mostly comes from the initialization period, the fixing rate also indicates the performance of TTFF.

In this case, it is evident that the fixing rate of GPS-only long baseline RTK is quite low. For the baseline at 60 km, the fixing rate is only 43.5 %, which implies that the mean TTFF is approximately 16.9 min. When QZSS is combined, this value could dramatically improve to 4.8 min. For other baselines, it shows similar results and the mean TTFF

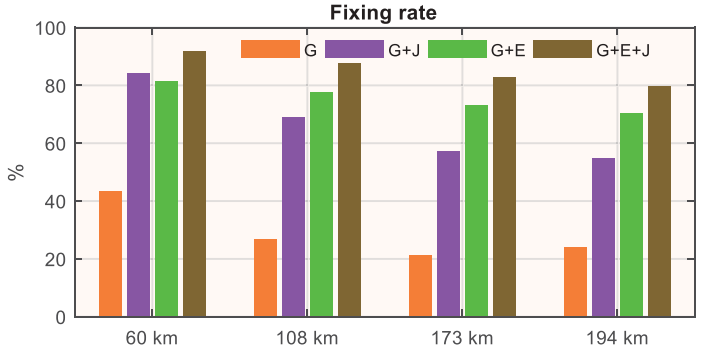

Figure 12. Fixing rate for the four baselines of different GNSS combination.

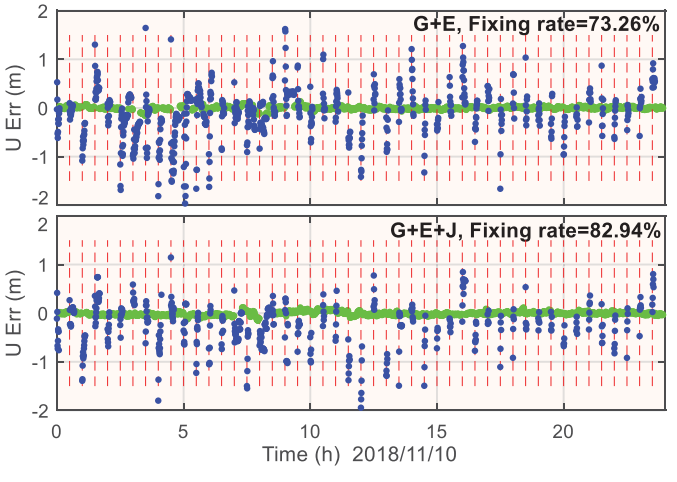

Figure 13. RTK solution in the Up direction for the 173 km baseline of GPS+Galileo (top) and GPS +Galileo+QZSS (bottom). The green point represents the fixed solution, the blue point represents the float solution, and the red dashed line separates every 30 min re-initialization session.

improves from 21.3 min to 10.1 min for GPS when combined with QZSS. This is worse than the ADOP convergence performance analyzed in Figure 9. As for GPS+Galileo, the mean TTFF is 7.3 min, which then decreases to 4.3 min after combining with QZSS. Unlike ADOP performance, the contribution of QZSS on TTFF is not as good as Galileo on GPS. This may due to the difference between model and real data. As ADOP is an ideal model that based on the covariance matrix and assuming that the observation errors follows standard Gaussian distribution. Therefore, ADOP may indicate the AR performance, but is still different from real AR performance using real data. Generally, with the increase of baseline length, the TTFF performance decreases slightly, which is expectable given that the constraint model of ionosphere and troposphere may be less accurate.

4.4. Instantaneous RTK

Instantaneous RTK or single epoch RTK is also a method to assess RTK performance. It can be regarded as an extreme situation of TTFF. If correct AR could be derived from one single epoch, it implies that the TTFF is zero. For short baseline RTK, instantaneous single epoch AR is easy to achieve using multi-GNSS or multi-frequency data (Odolinski *et al*. 2015a). However, in the case of long baseline RTK, single epoch RTK is almost impossible with a reliable success rate of 0.99 because the ADOP value needs time to convergence to 0.14 cycles (Odolinski *et al*. 2014). This can also be verified in Figure 9. Therefore, for the test of instantaneous RTK, we set the minimum success rate as zero, which implies that the success rate is not considered, and we only rely on the ratio test. Although this may lead to wrong fixed results, based on experience, a wrong fixed solution is usually better than a float solution.

We apply instantaneous RTK in the long baseline to evaluate the contribution of QZSS for this kind of RTK mode. Given that the success rate is not considered, the indicator of the fixing rate is no longer persuasive, so we only focus on positioning accuracy. To evaluate the positioning accuracy, the percentage of the expected three-dimension (3D) positioning error is calculated. Figures 14 and 15 depict the accumulation of 3D positioning error for different GNSS combination of four baselines. It is evident that using QZSS, positioning accuracy of instantaneous RTK would dramatically improve. Compared with GPS or GPS+Galileo, the accuracy of the 95% confidence level would improve by a factor of two when QZSS is utilized, which indicates that it contributes a more stable positioning result in the instantaneous RTK mode. It is promising to see that decimeter positioning accuracy can be achieved for the GPS+Galileo+QZSS combination at the 95% confidence level. Meanwhile, for 60 km baseline, the trend of positioning error accumulation is steeper, which is attributed to the higher fixing rate.

5. Conclusions

In this study, we present the triple frequency long baseline RTK algorithm. This algorithm exploits the geometry-free based instantaneous EWL AR and fast geometry-based WL AR. To improve the ADOP value of raw observations based on the long baseline RTK, the impact of orbit, troposphere and ionosphere difference is analyzed and some appropriate constraints should be added to the function model. Based on the analysis of the results, it is concluded that the influence of broadcast orbit could be ignored for baselines within

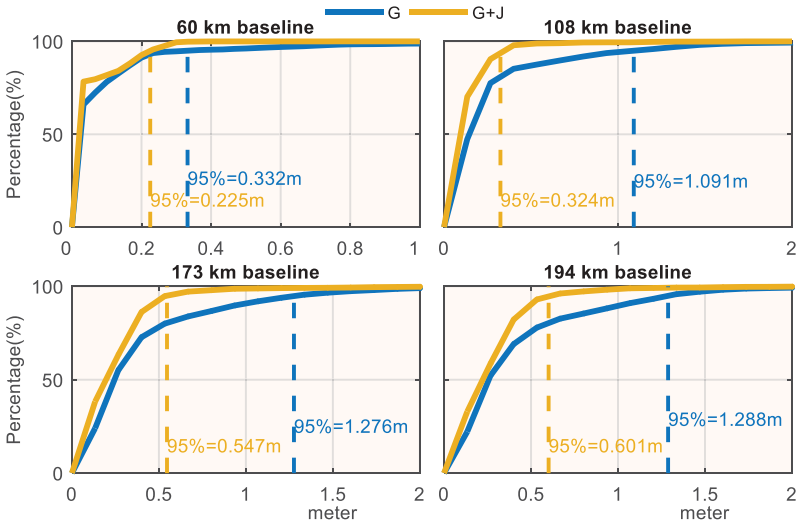

Figure 14. Percentage of the expected 3D position error of GPS (G) and GPS+QZSS (G+J) for four baselines. The corresponding dash line indicates the error at 95% confidence level.

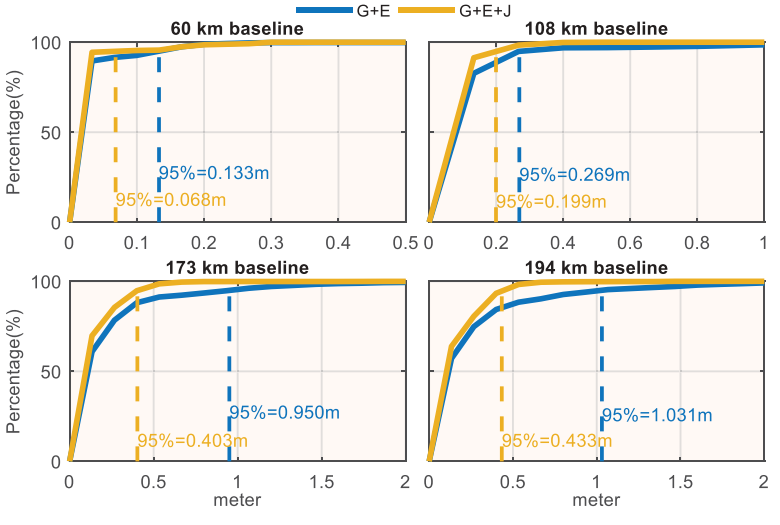

Figure 15. Percentage of the expected 3D position error of GPS+Galileo (G+E) and GPS+Galileo +QZSS (G+E+J) for four baselines. The corresponding dash line indicates the error at 95% confidence level.

200 km. For troposphere and ionosphere difference, it should be estimated as the random walk parameter in the Kalman Filter. A model of the troposphere and ionosphere constraint and random walk step is proposed in this contribution.

The analysis of the results proves that using QZSS, the satellite number and PDOP value improve in the service region of QZSS, especially over Japan. Given that 3–4 satellites are always visible in Japan, the ADOP value convergences faster, which indicates a faster convergence and AR performance for long baseline RTK.

Using the data of GPS+Galileo+QZSS for different baseline lengths near Tokyo, long baseline RTK results show that QZSS would improve the positioning accuracy and fixing rate. The overall precision is better than 2 cm in the horizontal and 4 cm in the vertical in RMS and the fixing rate is higher than 97%. In terms of the convergence performance, the TTFF also improves with the contribution of QZSS, especially for the GPS-only case. In addition, QZSS also benefits instantaneous long baseline RTK, which can achieve decimeter positioning accuracy with a 95% confidence level using only one single epoch data in combination with GPS+Galileo.

However, the results are based on four baselines analysis. Given that the difference, especially in the case of the ionosphere varies in time and space. More data and analysis should be conducted to obtain a more complete understanding of QZSS in long baseline RTK. Nevertheless, this study has demonstrated the significance of the contribution of QZSS in RTK. With a high elevation and long visible period of QZSS in Japan, the contribution of QZSS is very promising in an urban environment, especially in the case of an urban canyon.

Disclosure statement

No potential conflict of interest was reported by the authors.

Funding

This work was supported by the National Natural Science Foundation of China [No. 41874042]; Opening Project of Shanghai Key Laboratory of Space Navigation and Positioning Techniques [No. KFKT_201705].

References

Böhm, J., *et al*., 2015. Development of an improved empirical model for slant delays in the troposphere (GPT2w). *GPS Solutions*, 19 (3), 433–441. doi:10.1007/s10291-014-0403-7

Chu, F.Y. and Yang, M., 2014. GPS/Galileo long baseline computation: method and performance analyses. *GPS Solutions*, 18 (2), 263–272. doi:10.1007/s10291-013-0327-7

Chu, F.Y., Yang, M., and Wu, J., 2016. A new approach to modernized GPS phase-only ambiguity resolution over long baselines. *Journal of Geodesy*, 90 (3), 241–254. doi:10.1007/s00190-015-0869-2

Feng, Y., 2008. GNSS three carrier ambiguity resolution using ionosphere-reduced virtual signals. *Journal of Geodesy*, 82 (12), 847–862. doi:10.1007/s00190-008-0209-x

Feng, Y. and Li, B., 2008. A benefit of multiple carrier GNSS signals: regional scale network-based RTK with doubled inter-station distances. *Journal of Spatial Science*, 53 (2), 135–147. doi:10.1080/14498596.2008.9635154

Foster, J.C., 2000. Quantitative investigation of ionospheric density gradients at mid latitudes. *In*: *Proceedings of the Institute of Navigation ION 2000 conference*, Anaheim, CA, January 2000, pp. 447–453.

Gao, W., *et al*., 2015. Improving ambiguity resolution for medium baselines using combined GPS and BDS dual/triple-frequency observations. *Sensors*, 15 (11), 27525–27542. doi:10.3390/s151127525

Hou, Y., Verhagen, S., and Wu, J., 2016. A data driven partial ambiguity resolution: two step success rate criterion, and its simulation demonstration. *Advances in Space Research*, 58 (11), 2435–2452. doi:10.1016/j.asr.2016.07.029

JAXA, 2017. *Interface specification for QZSS(IS-QZSS)*. Technical report, October 2016, 197 pp.
Kitamura, M., Ota, T., and Amano, A.Y., 2014. Improving availability and accuracy of multi-GNSS positioning using QZSS. *In*: *Proceedings of the 27th International Technical Meeting of the Satellite Division of The Institute of Navigation (ION GNSS+ 2014)*, September 2014, Tampa, Florida. 2341–2345
Kubo, N., *et al*., 2011. Performance evaluation of the effect of QZS (Quasi-Zenith Satellite) on precise positioning. *Coordinates*, 7 (7), 7–13.
Li, B., Feng, Y., and Shen, Y., 2010a. Three carrier ambiguity resolution: distance-independent performance demonstrated using semi-generated triple frequency GPS signals. *GPS Solutions*, 14 (2), 177–184. doi:10.1007/s10291-009-0131-6
Li, B., *et al*., 2010b. Geometry-specified troposphere decorrelation for subcentimeter real-time kinematic solutions over long baselines. *Journal of Geophysical Research Solid Earth*, B11404.
Li, B., *et al*., 2014. GNSS ambiguity resolution with controllable failure rate for long baseline network RTK. *Journal of Geodesy*, 88 (2), 99–112. doi:10.1007/s00190-013-0670-z
Li, G., *et al*., 2017. Double differencing within GNSS constellations. *GPS Solutions*, 21 (3), 1161–1177. doi:10.1007/s10291-017-0599-4
Montenbruck, O., *et al*., 2017. The Multi-GNSS Experiment (MGEX) of the International GNSS Service (IGS)–achievements, prospects and challenges. *Advances in Space Research*, 59 (7), 1671–1697. doi:10.1016/j.asr.2017.01.011
Odijk, D., 2000. Weighting ionospheric corrections to improve fast GPS positioning over medium distances. *In*: *Proceedings of International Technical Meeting of the Satellite Division of the Institute of Navigation*, Salt Lake City, UT, September 2000, pp. 1113–1123.
Odijk, D., *et al*., 2017. GPS, Galileo, QZSS and IRNSS differential ISBs: estimation and application. *GPS Solutions*, 21 (2), 439–450. doi:10.1007/s10291-016-0536-y
Odijk, D. and Teunissen, P.J.G., 2008. ADOP in closed form for a hierarchy of multi-frequency single-baseline GNSS models. *Journal of Geodesy*, 82 (8), 473. doi:10.1007/s00190-007-0197-2
Odijk, D. and Teunissen, P.J.G., 2013. Estimation of differential intersystem biases between the overlapping frequencies of GPS, Galileo, BeiDou and QZSS. *In*: *Proceedings of 4th international colloquium scientific and fundamental aspects of the Galileo programme*, 4–6 December, Prague, Czech Republic, 8.
Odolinski, R. and Teunissen, P.J.G., 2017. Low-cost, 4-system, precise GNSS positioning: a GPS, Galileo, BDS and QZSS ionosphere-weighted RTK analysis. *Measurement Science and Technology*, 28, 125801. doi:10.1088/1361-6501/aa92eb
Odolinski, R., Teunissen, P.J.G., and Odijk, D., 2014. Combined GPS+ BDS+ Galileo+ QZSS for long baseline RTK positioning. *In*: Proceedings of ION GNSS (pp. 2326–2340). *Proceedings of the 27th International Technical Meeting of the Satellite Division of The Institute of Navigation (ION GNSS+ 2014)*, Tampa, Florida, September 2014, pp. 2341–2345.
Odolinski, R., Teunissen, P.J.G., and Odijk, D., 2015a. Combined BDS, Galileo, QZSS and GPS single-frequency RTK. *GPS Solutions*, 19 (1), 151–163. doi:10.1007/s10291-014-0376-6
Odolinski, R., Teunissen, P.J.G., and Odijk, D., 2015b. Combined GPS+BDS for short to long baseline RTK positioning. *Measurement Science and Technology*, 26 (4), 045801. doi:10.1088/0957-0233/26/4/045801
Parkins, A., 2011. Increasing GNSS RTK availability with a new single-epoch batch partial ambiguity resolution algorithm. *GPS Solutions*, 15 (4), 391–402. doi:10.1007/s10291-010-0198-0
Takasu, T., Ebinuma, T., and Yasuda, A., 2009. Effect of quasi zenith satellite (QZS) on GPS positioning. *In*: *Proceedings of 2009 International Symposium on GPS/GNSS*, Jeju, Korea.
Takasu, T. and Yasuda, A., 2010. Kalman-Filter-based integer ambiguity resolution strategy for long-baseline RTK with ionosphere and troposphere estimation. *Proceedings of International Technical Meeting of the Satellite Division of the Institute of Navigation*, 7672 (6), 161–171.
Teunissen, P. and Montenbruck, O., Eds., 2017. *Springer handbook of global navigation satellite systems*. Gewerbestrasse, Switzerland: Springer.
Teunissen, P.J., 1997. A canonical theory for short GPS baselines. Part IV: precision versus reliability. *Journal of Geodesy*, 71 (9), 513–525. doi:10.1007/s001900050119

Teunissen, P.J.G., 1995. The least-squares ambiguity decorrelation adjustment: a method for fast GPS integer ambiguity estimation. *Journal of Geodesy*, 70 (1–2), 65–82. doi:10.1007/BF00863419

Teunissen, P.J.G., Joosten, P., and Tiberius, C.C.J.M., 1999. Geometry-free ambiguity success rates in case of partial fixing, *In*: *Proc. of ION National Technical Meeting 1999 & 19th Biennal Guidance Test Symposium*, San Diego CA, pp. 201–207.

Verhagen, S. and Li, B., 2012. *LAMBDA software package: matlab implementation, Version 3.0*. Perth, Australia: Delft University of Technology and Curtin University.

Verhagen, S. and Teunissen, P.J.G., 2013. The ratio test for future GNSS ambiguity resolution. *GPS Solutions*, 17 (4), 535–548. doi:10.1007/s10291-012-0299-z

Wanninger, L., 1993. Effects of equatorial ionosphere on GPS. *GPS World*, 4 (7), 48–52.

Wanninger, L., 2012. Carrier-phase inter-frequency biases of GLONASS receivers. *Journal of Geodesy*, 86 (2), 139–148. doi:10.1007/s00190-011-0502-y

Zaminpardaz, S., Wang, K., and Teunissen, P.J., 2018. Australia-first high-precision positioning results with new Japanese QZSS regional satellite system. *GPS Solutions*, 22 (4), 101. doi:10.1007/s10291-018-0763-5

Zhang, Q., *et al*., 2018b. Performance evaluation of QZSS augmenting GPS and BDS single-frequency single-epoch positioning with actual data in Asia-Pacific region. *ISPRS International Journal of Geo-Information*, 7 (5), 186. doi:10.3390/ijgi7050186

Zhang, S., *et al*., 2016. A sequential and partial ambiguity resolution strategy for improving the initialization performance of medium-baseline relative positioning. *Earth, Planets and Space*, 68 (1), 29. doi:10.1186/s40623-016-0411-7

Zhang, Y., *et al*., 2018a. Assessment of the contribution of QZSS combined GPS/BeiDou positioning in Asia-Pacific Areas. *China Satellite Navigation Conference (CSNC) 2018 Proceedings (Vol. 1)*. Harbin, China: Springer, 467–478.